Continuum constitutive laws to describe acoustic attenuation in glasses

H. Luo and A. Gravouil
LaMCos, INSA-Lyon, CNRS UMR5259, Université de Lyon, F-69621 Villeurbanne Cedex, France

V. M. Giordano
Institut Lumière Matière, UMR 5306 Université Lyon 1-CNRS, F-69622 Villeurbanne Cedex, France

W. Schirmacher
Institut für Physik, Universität Mainz, Staudinger Weg 7, D-55099 Mainz, Germany

A. Tanguy
LaMCos, INSA-Lyon, CNRS UMR5259, Université de Lyon, F-69621 Villeurbanne Cedex, France
and ONERA, University Paris-Saclay, Chemin de la Huniére, BP 80100, 92123 Palaiseau, France

(Received 13 June 2020; accepted 19 August 2020; published 14 September 2020)

Nowadays metamaterials are at the focus of an intense research as promising for thermal and acoustic engineering. However, the computational cost associated to the large system size required for correctly simulating them imposes the use of finite-elements simulations, developing continuum models, able to grasp the physics at play without entering in the atomistic details. Still, a correct description should be able to reproduce not only the extrinsic scattering sources on waves propagation, as introduced by the metamaterial microstructure, but also the intrinsic wave attenuation of the material itself. This becomes dramatically important when the metamaterial is made out of a glass, which is intrinsically highly dissipative and with a wave attenuation strongly dependent on frequency. Here we propose a continuum mechanical model for a viscoelastic medium, able to bridge atomic and macroscopic scale in amorphous materials and describe phonon attenuation due to atomistic mechanisms, characterized by a defined frequency dependence. This represents a first decisive step for investigating the effect of a complex nano- or microstructure on acoustic attenuation, while including the atomistic contribution as well.

DOI: 10.1103/PhysRevE.102.033003

I. INTRODUCTION

Nowadays, a large technological interest is focusing on the potential of heterogeneous architectured materials for a number of applications [1]. These are manmade structural materials which have been developed for obtaining *ad hoc* properties, that cannot be generally found in nature. They are generally obtained by engineering at different scales the mixing of different materials, either in a random spacial distribution (composite materials) either with the artificial repetition of regular patterns (metamaterials). Depending on their application, the lengthscale of such patterns can span from the nanometer to the macroscopic range, being smaller than the wavelength of the phenomena that the material is meant to affect.

Metamaterials have been largely investigated for applications in acoustics, where they can be shaped to realize acoustic guides, filters, lenses, with a macrostructure in a macroscopic lengthscale [2–5]. More recently, thanks to both engineering and theoretical progresses, they have been introduced also in thermal science, with a microstructure in the nanometer scale, for realizing tunable multi-functional thermal metamaterials [6,7], thermal cloaks and camouflage [8], etc. In both applications, it is matter of guiding, filtering, hindering, the propagation of acoustic waves (phonons), responsible for the sound propagation when their wavelength is macroscopic, and for thermal transport at room temperature when it is nanometric.

A heterogeneous architectured material perturbs the propagation of the acoustic waves by introducing an extrinsic source of scattering, represented by the interfaces. In the specific case of metamaterials novel coherent effects arise, due to their periodicity. Because of this latter, a new Brillouin Zone can be defined, which strongly modifies the phonon band structure by folding the dispersions at its boundaries, thus introducing new optic modes which can scatter the acoustic ones. Moreover, the presence of elemental bricks in the micro-structure with a proper resonant frequency introduces interference effects with phonons, leading to the aperture of forbidden gaps in the phonon dispersion [2,3], useful for the realization of acoustic filters and for impacting thermal transport [9].

To study the acoustic wave propagation and attenuation in such complex structured materials, it is necessary to model phonon propagation on large scale systems, more apt at representing real materials, where the effect of heterogeneities and interfaces can be properly investigated. Such large systems are out of reach for atomistic simulations, where the computing time scales with the atoms number as N^2 for a pair

 ©2020 American Physical Society

potential interaction, and even more for a multi-body interaction. Instead, a continuous model is expected to obtain the effective mechanical behavior without knowing the atomistic details. Its computing time depends on spatial discretization [10–13], making thus affordable longer simulations on larger systems. However, a correct description of phonon attenuation in heterogeneous architectured materials requires to take into account not only the extrinsic scattering sources introduced by the micro-structure, but also the intrinsic attenuation in the component materials. This is even more important when these latter are highly dissipative, as it is the case for amorphous materials, whose interest as building blocks for metamaterials efficient for thermal transport reduction has been recently recognized [9,14].

A multiscale approach is therefore needed, able to connect the atomistic scale, where the intrinsic phonon attenuation takes its origin, and the macroscopic scale, where the metamaterial assembly introduces the extrinsic scattering sources. Moreover, such model should be able to reproduce the frequency dependence of the intrinsic acoustic attenuation, which is specific to the microscopic mechanisms at play.

In glasses, many attenuation channels are present, whose importance depends on phonon frequency and temperature: tunneling due to two level systems [15], soft modes [16], thermally activated relaxation processes [17], anharmonicity [18], and scattering induced by structural disorder [19–21]. This last contribution is temperature independent, and dominates acoustic attenuation at frequencies in the GHz-THz range [22]. For lower frequencies, anharmonicity gives rise to a phonon attenuation, or damping, Γ, inversely proportional to phonon lifetime, which changes with frequency as ω^2. Approaching the THz range, corresponding to phonon wavelengths in the nanometer scale, scattering on disorder starts to dominate, characterized by a Rayleigh-like dependence $\Gamma \propto \omega^4$, with a progressive transition to a strong scattering regime, finally leading to a new high frequency $\Gamma \propto \omega^2$ regime, as reported in a number of experimental and theoretical studies [17,23–30]. This strong scattering takes place at frequencies comparable with the Boson Peak, i.e., the excess of modes in the phonon density of states with respect to the Debye prediction at low frequency, and has been explained as due to phonon scattering by nanometric elastic heterogeneities [29–35]. At low temperature, molecular-dynamics (MD) simulations have been able to reproduce this attenuation crossover, with some different scaling rules [19,21,34,36,37]. The addition of anharmonicity at finite temperatures has finally provided a complete picture of combination of the different attenuation channels [25,38].

On the whole, three regimes of acoustic attenuation versus frequency can be classified: (1) $\Gamma \propto \omega^2$ due to the anharmonicity at low frequencies, with a temperature-dependent strength; (2) $\Gamma \propto \omega^4$ due to Rayleigh-like scattering induced by disorder and leading to a dramatic phonon lifetime reduction, so that the collective vibrational modes loose progressively their plane wave character; (3) $\Gamma \propto \omega^2$ above Ioffe-Regel frequency ($\omega_{\mathrm{IR}} = \pi\Gamma$), where phonons cannot be considered as a propagative plane waves anymore. As such, they do not propagate anymore but are diffusive, and, at higher frequency, even localized [19,20,39].

To correctly describe an amorphous-based metamaterial, we thus need to connect atomistic and macroscopic scale, keeping the information on the active intrinsic attenuation channel and the microscopic frequency and temperature dependence of phonon attenuation. Generally speaking, there exist two strategies for a multiscale approach: *hierarchical* and *concurrent* [40]. The idea of *hierarchical* scale-bridging techniques is to extract information at the microscale for identifying an effective behavior to be used as an input at larger scales. Typical examples are the use of an Eshelby inclusion to describe the quadrupolar stress map of the shear transformation zone induced by plasticity in some amorphous materials (STZ) [41–43], or the use of mesoscopic viscoplastic models to reproduce the bulk rheology [44]. Other methods involve a physically based coarse-graining of the mechanical properties [45–47], and measurement of the effective constitutive laws at different scales [48] to be implemented in finite-element (FE) simulations [49], as successfully applied for simulating the elastoplastic behavior of silica micropillars [49]. However, accounting for properties that change with time and frequency (dynamic homogenization) still poses challenges: This is the case of transient sound attenuation [40,50].

In this work we propose to develop a model to homogenize the effective attenuation triggered by multiple mechanisms, and characterized by a defined frequency dependence. To this aim, we start from the viscous attenuation of acoustic waves in compressible Newtonian fluids, as formulated within Stoke's theory [51]: the amplitude of a plane wave decreases exponentially with the propagation distance, with a decay rate given, in the low frequency limit $\omega\tau \ll 1$, by $\alpha = \frac{\omega^2\tau}{2v}$, with $\tau = \frac{4\eta}{3\rho v^2}$, where η is the dynamic viscosity coefficient, ρ is the fluid density and v is the speed of sound in the absence of viscosity. This behavior yields to a typical attenuation distance $l = 1/\alpha$ scaling as $\propto\omega^{-2}$. A similar exponential attenuation of acoustic wave packets was also evidenced in amorphous materials below the Ioffe-Regel frequency [20], allowing defining a mean-free path from the corresponding Beer-Lambert law for acoustic transport attenuation. This behavior is thus similar in amorphous materials and in Newtonian liquids. Glasses can be thus characterized by an effective viscoelastic behavior for their acoustic properties, even below the glass transition temperature (that is, in the solid state). This corresponds also to the requirement that the internal friction in the material can be characterized by the quality factor $Q^{-1} = G''/G'$ where $G = G' + iG''$ is the complex elastic modulus in the linear regime [15]. This is indeed the case in a glass [22] for frequencies below the Ioffe-Regel crossover, where acoustic phonons (named propagons [39]) still maintain well-defined wave vectors and exhibit an exponential decay. A relation can be found between the microscopic quantity (phonon attenuation) and the macroscopic one (quality factor): $\Gamma/\omega = Q^{-1}$ [22,35,52–55].

We therefore develop here a new continuum mechanical model for a viscoelastic medium, where no disorder is introduced. We will show that this model is able to bridge atomic and macroscopic scale in amorphous materials and describe phonon attenuation, in this work taken with a ω^2 dependency, in a prototype material, amorphous silicon, at wavelengths at which phonon attenuation has an atomistic origin. As such

our model proves to be able to give a continuum description of atomistic processes, valid for out-of-equilibrium transient transport of energy (acoustic attenuation), as well as for a general description of the effective mechanical behavior of disordered heterogeneous materials.

In the following, in Sec. II we present our viscoelastic model and calibrate it against amorphous silicon. In Sec. III, we detail the numerical methods used to verify its validity through the study of the propagation of wave packets in such medium. Such study will be presented in detail, as a function of the wave-packet frequency, in Sec. IV, and compared with results from molecular dynamics (MD) simulations. Secs. V and VI are devoted to discussion and conclusion.

II. SIMPLE CONSTITUTIVE MODEL FOR LONGITUDINAL AND TRANSVERSE ATTENUATION IN GLASSES

The first step for describing large-scale amorphous-based metamaterials consists in developing a continuum model able to reproduce the intrinsic attenuation in the amorphous component. As mentioned in the Introduction, phonon attenuation in glasses is due to different mechanisms, depending on the phonon energy and temperature. We are here interested to phonons with energies in the THz range and wavelengths in the nm range, which dominate thermal transport at room temperature. At such energies the dominant scattering source is the structural disorder [17,38]. In this section, we will develop a viscoelastic model to describe this disorder-induced harmonic damping in the THz regime. We will derive the mechanical response both in frequency and time domain. The frequency-dependent response allows to obtain the analytic expression for the figure of merit Q^{-1}, which is related to the phonon attenuation below the Ioffe-Regel crossover, as $Q^{-1} = \Gamma/\omega$. The time-domain one corresponds to the so-called stress-strain constitutive law, that we need for running finite-element method (FEM) simulations for investigating the wave-packet propagation at large scale.

Let us assume an isotropic, homogeneous, and viscous solid: we can express the elastic constitutive laws describing the stress-strain relation using the Hooke's law and separating the hydrostatic from the deviatoric components:

$$\sigma_{ij} = 3K\epsilon_{ij}^{\mathrm{sph}} + 2G\epsilon_{ij}^{\mathrm{dev}} \tag{1}$$

where K is the bulk modulus and G is the shear modulus. The hydrostatic (or spherical) part of strain is given by $\epsilon_{ij}^{\mathrm{sph}} = \frac{1}{3}\delta_{ij}\epsilon_{kk}$ and the deviatoric part, which is isochoric, is $\epsilon_{ij}^{\mathrm{dev}} = \epsilon_{ij} - \frac{1}{3}\delta_{ij}\epsilon_{kk}$, where δ_{ij} is Dirac function. Stress respects the same separation rule, and can be written as

$$\begin{cases} \sigma_{ij}^{\mathrm{sph}} & = \frac{1}{3}\delta_{ij}\sigma_{kk} = 3K\epsilon_{ij}^{\mathrm{sph}}, \\ \epsilon_{ij}^{\mathrm{dev}} & = \sigma_{ij} - \frac{1}{3}\delta_{ij}\sigma_{kk} = 2G\epsilon_{ij}^{\mathrm{dev}}. \end{cases} \tag{2}$$

The interest of such separation is that in the following we will use different rheological models: a Kelvin-Voigt (K-V) approach for the hydrostatic part and a Maxwell-like model for the deviatoric one, as illustrated in Fig. 1.

This latter model gives indeed a good description of the rheological constitutive relation [56]. Here, we use the simplest version of the generalized Maxwell model called the

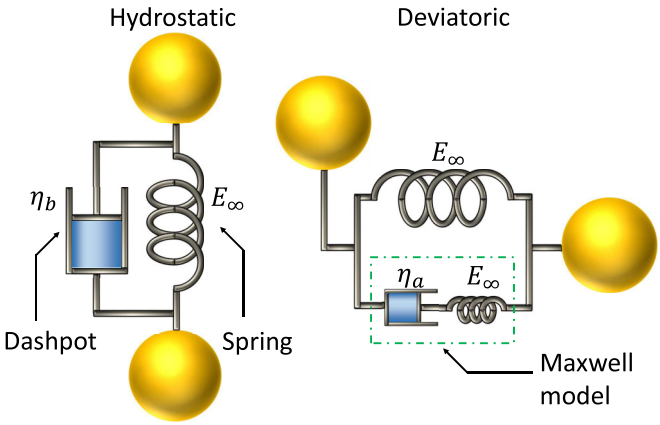

FIG. 1. Illustration of the viscoelastic models: the Kelvin-Voigt model for the hydrostatic part and the standard linear model (one type of the generalized Maxwell model with $N = 1$) for the deviatoric part.

standard linear model [57] as shown in Fig. 1 (right panel). The idea behind this model is that the deviatoric part will generate a viscous flow limited by the elasticity of the solid. The time-dependent stress-strain relation following the Standard linear model reads

$$\sigma_{ij}^{\mathrm{dev}}(t) + \tau_a\dot{\sigma}_{ij}^{\mathrm{dev}}(t) = E_a\epsilon_{ij}^{\mathrm{dev}}(t) + 2E_a\tau_a\dot{\epsilon}_{ij}^{\mathrm{dev}}(t), \tag{3}$$

where $\tau_a = \eta_a/E_a$ is the relaxation time, η_a is the viscosity, and E_a is the shear modulus. Supposing that nothing happens before $t = 0$, Eq. (3) can be written on a complex plane by means of a Laplace transform:

$$(1 + \tau_a s)\mathscr{L}\left[\sigma_{ij}^{\mathrm{dev}}(t)\right](s) = (E_a + 2E_a\tau_a s)\mathscr{L}\left[\epsilon_{ij}^{\mathrm{dev}}(t)\right](s), \tag{4}$$

with $s = i\omega + \xi$ the Laplace frequency parameter (with $\xi \to 0$). We can then define the transfer function between strain and stress:

$$\frac{\mathscr{L}\left[\sigma_{ij}^{\mathrm{dev}}(t)\right](s)}{\mathscr{L}\left[\epsilon_{ij}^{\mathrm{dev}}(t)\right](s)} = E_a\left(1 + \frac{\tau_a s}{1 + \tau_a s}\right). \tag{5}$$

Replacing s, we obtain the expression of the complex elastic modulus $E_A^*(\omega) = E_A'(\omega) + iE_A''(\omega)$ for the Standard linear model:

$$\begin{aligned} E_A^*(\omega) &= \left.\frac{\mathscr{L}\left[\sigma_{ij}^{\mathrm{dev}}(t)\right](s)}{\mathscr{L}\left[\epsilon_{ij}^{\mathrm{dev}}(t)\right](s)}\right|_{s=i\omega+\xi} \\ &= E_a\left(1 + \frac{i\omega\tau_a}{1 + i\omega\tau_a}\right). \end{aligned} \tag{6}$$

For the hydrostatic part, we use the Kelvin-Voigt model (left panel in Fig. 1). This is motivated by the fact that the hydrostatic part will mainly give rise to a delayed response, without inducing a macroscopic flow. For this reason, the rheologic contribution from the hydrostatic part is often neglected [58], the deviatoric contribution being much more significant at large times. Still, a more precise description of the attenuation can be obtained if it is taken into account [59]. K-V stress-strain relation can be expressed as

$$\sigma_{ij}^{\mathrm{sph}}(t) = E_b\left[\epsilon_{ij}^{\mathrm{sph}}(t) + \tau_b\dot{\epsilon}_{ij}^{\mathrm{sph}}(t)\right], \tag{7}$$

where $\tau_b = \eta_b/E_b$ with E_b the bulk modulus.

Similar to the Standard linear model, the transfer function of K-V model is given by

$$\frac{\mathscr{L}\left[\sigma_{ij}^{\mathrm{sph}}(t)\right](s)}{\mathscr{L}\left[\epsilon_{ij}^{\mathrm{sph}}(t)\right](s)} = E_b(1+\tau_b s), \tag{8}$$

which allows us to define the complex modulus:

$$E_B^*(\omega) = E_b(1+i\omega\tau_b). \tag{9}$$

It is straightforward to link such expressions to Eq. (2) by simply replacing the elastic moduli $3K$ and $2G$ by their viscoelastic analogues of the trace part, i.e., E_B^*, and the deviatoric part, i.e., E_A^*, respectively [57]. In the low-frequency limit ($\omega \to 0$), it should be

$$\begin{cases} E_A^*(\omega\to 0) = E_a\left(1+\frac{i\omega\tau_a}{1+i\omega\tau_a}\right)|_{\omega\to 0} = 2G, \\ E_B^*(\omega\to 0) = E_b(1+i\omega\tau_b)|_{\omega\to 0} = 3K, \end{cases} \tag{10}$$

which leads to the following identities:

$$\begin{cases} E_a = 2G = \frac{E}{1+\nu}, \\ E_b = 3K = \frac{E}{1-2\nu}, \end{cases} \tag{11}$$

where E is the Young modulus and ν is the Poisson ratio.

We can now write down the full complex constitutive elastic tensor $\mathbb{G}^*$, including hydrostatic and deviatoric components. Due to isotropy, this tensor is reduced to a 6×6 symmetric matrix, imposing the conditions $G_{11}^* = G_{22}^* = G_{33}^*$ and $G_{44}^* = G_{55}^* = G_{66}^*$, where G_{ij}^* is the ith row and jth column. These 6 elements can thus be expressed in terms of only four parameters (E, ν, τ_a, and τ_b), as detailed in the Appendix:

$$\mathbb{G}^* = \begin{bmatrix} \frac{E_B^*+2E_A^*}{3} & \frac{E_B^*-E_A^*}{3} & \frac{E_B^*-E_A^*}{3} & 0 & 0 & 0 \\ \frac{E_B^*-E_A^*}{3} & \frac{E_B^*+2E_A^*}{3} & \frac{E_B^*-E_A^*}{3} & 0 & 0 & 0 \\ \frac{E_B^*-E_A^*}{3} & \frac{E_B^*-E_A^*}{3} & \frac{E_B^*+2E_A^*}{3} & 0 & 0 & 0 \\ 0 & 0 & 0 & \frac{1}{2}E_A^* & 0 & 0 \\ 0 & 0 & 0 & 0 & \frac{1}{2}E_A^* & 0 \\ 0 & 0 & 0 & 0 & 0 & \frac{1}{2}E_A^* \end{bmatrix}, \tag{12}$$

with E_A^* and E_B^* given in Eqs. (6), (9), and (11).

To obtain the stress-strain constitutive law we need to solve the time-domain expressions given in Eqs. (3) and (7), reminding that the total stress is $\sigma_{ij} = \sigma_{ij}^{\mathrm{sph}} + \sigma_{ij}^{\mathrm{dev}}$. For the deviatoric part, solution of Eq. (3) is

$$\sigma_{ij}^{\mathrm{dev}}(t) = E_a\left[\epsilon_{ij}^{\mathrm{dev}} + \int_0^t \exp\left(-\frac{t-t'}{\tau_a}\right)\frac{\partial\epsilon_{ij}^{\mathrm{dev}}}{\partial t'}dt'\right]. \tag{13}$$

Combining Eqs. (7), (13), and (11), the stress-strain constitutive law then reads

$$\sigma_{ij}(t) = \frac{E}{1-2\nu}\left(\epsilon_{ij}^{\mathrm{sph}} + \tau_b\frac{\partial\epsilon_{ij}^{\mathrm{sph}}}{\partial t}\right) + \frac{E}{1+\nu}\left[\epsilon_{ij}^{\mathrm{dev}} + \int_0^t \exp\left(-\frac{t-t'}{\tau_a}\right)\frac{\partial\epsilon_{ij}^{\mathrm{dev}}}{\partial t'}dt'\right]. \tag{14}$$

Our approach for solving the convolution integral in Eq. (14) is to introduce an internal variable tensor h_{ij} [58,60] whose evolution indirectly includes the mechanical history of a material. We reformulate Eq. (14) as

$$\sigma_{ij}(t) = \frac{E}{1-2\nu}\left(\epsilon_{ij}^{\mathrm{sph}} + \tau_b\frac{\partial\epsilon_{ij}^{\mathrm{sph}}}{\partial t}\right) + \frac{E}{1+\nu}\epsilon_{ij}^{\mathrm{dev}} + h_{ij}, \tag{15}$$

where $h_{ij}(t)$ is defined by a recurrence relation:

$$h_{ij}(t) = \exp\left(-\frac{t-t_n}{\tau_a}\right)h_{ij}(t_n) + \frac{E}{1+\nu}\int_{t_n}^t \exp\left(-\frac{t-t'}{\tau_a}\right)\frac{\partial\epsilon_{ij}^{\mathrm{dev}}}{\partial t'}dt', \tag{16}$$

where t_n is any moment before t. As such, instead of computing the convolution integral from 0, we only need to integrate from t_n to t if $h_{ij}(t_n)$ is known.

III. FINITE-ELEMENT SIMULATIONS

Equation (14) only depends on four material parameters, two of them related to elasticity (E and ν) and two to viscoelasticity (τ_a and τ_b). To use it for running a finite-element simulation on a given material, these quantities need to be fixed to the ones of the material under investigation. To this aim, we derive from the elastic tensor the longitudinal and transverse quality factors and acoustic waves velocities, to be compared with the same quantities extracted from experiments or atomistic numerical simulations, to fix the four parameters.

By definition, isotropic longitudinal (L) and transverse (T) sound speeds are defined as

$$\begin{cases} v_L(\omega)^2 &= \frac{G'_{11}(\omega)}{\rho}, \\ v_T(\omega)^2 &= \frac{G'_{44}(\omega)}{\rho}, \end{cases} \tag{17}$$

similarly, the quality factors are obtained as

$$Q_L^{-1}(\omega) = \frac{G''_{11}(\omega)}{G'_{11}(\omega)} \text{ and } Q_T^{-1}(\omega) = \frac{G''_{44}(\omega)}{G'_{44}(\omega)}, \tag{18}$$

where $G'_{ij} = \mathrm{Re}(G_{ij}^*)$ and $G''_{ij} = \mathrm{Im}(G_{ij}^*)$.

It is worth noticing that by construction this model describes $\Gamma \propto \omega^2$ energy-dependent attenuation, as can be verified by substituting G'' and G' in the $Q_{L,T}^{-1}$ expression. This behavior is in agreement with the energy dependence of acoustic attenuation in glasses as observed in experiments and numerical simulations at THz energies just above the Ioffe-Regel crossover. However, here the quality factor does not describe correctly the attenuation anymore, since it is well adapted only below the Ioffe-Regel criterion [22]. In the regime where phonon attenuation and quality factor can be related to each other, the former should go as ω^4. Still, this Rayleigh scattering regime is very short, and it makes the transition between two ω^2 dependencies, as described in the introduction. For this reason, as a first step for assessing the validity of our viscoelastic model, we propose to use a ω^2 dependence as a good empirical description even in this intermediate regime [19].

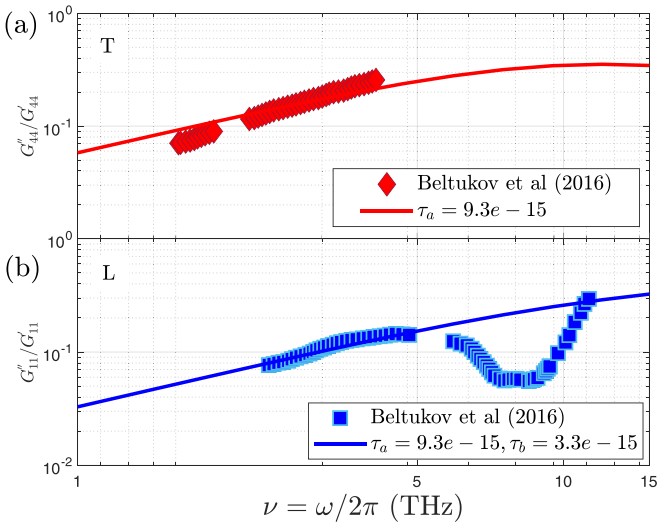

FIG. 2. Identification of parameters τ_a and τ_b by fitting $Q^{-1}_{L,T}$ against Γ/ω (data from Beltukov *et al.* [19]): (a) Evolution of $Q_T^{-1}(\omega)$ for transverse modes with $\tau_a = 9.3e-15$; (b) evolution of $Q_L^{-1}(\omega)$ for longitudinal modes with $\tau_a = 9.3e-15$ and $\tau_b = 3.3e-15$.

In the following, we will use this model for simulating wave-packet propagation in amorphous silicon, and compare the results with atomistic molecular dynamics simulations [19,20,61]. In those works, amorphous silicon is described by the Stillinger-Weber potential [62], where the three body parameter Λ is tuned for modifying the rigidity of the system. We compare here with the case $\Lambda = 21$, which gives a good description of real amorphous silicon, with mass density $\rho = 2303\,\mathrm{kg/m^3}$ [61].

E and ν are the macroscopic elastic properties, that we fix to the ones reported in Ref. [61]. τ_a and τ_b are found by fitting the frequency-dependent quality factor $Q^{-1} = \Gamma(\tau_a, \tau_b, \omega)/\omega$ against the one reported in Ref. [19] for longitudinal and transverse modes. Our best fits are reported in Fig. 2, together with the Γ/ω values from Ref. [19]. Optimal values for the relaxation times, together with the static values for the elastic parameters are reported in Table I.

As anticipated, the quality of the fit is limited by the approximation that we do in using a ω^2 law for representing the Rayleigh ω^4 dependence of acoustic attenuation, as clearly demonstrated by the departure of the model from the numerical data in the deviatoric part in Fig. 2(a). Moreover, in the trace part [Fig. 2(b)], a marked hollow is visible in the molecular dynamics measurements, which is not reproduced by our model, being due to the attenuation of the transverse waves above the Ioffe-Regel crossover.

It is worth stressing here that by calibrating our model onto the cited molecular dynamics simulations, we will investigate exactly the same system but representing it as a continuum medium, with no need of describing the interatomic interactions.

TABLE I. Parameters of the viscoelastic continuum model, fixed on atomistic molecular dynamics simulations.

E	ν	$\tau_a(10^{-15}s)$	$\tau_b(10^{-15}s)$
92.25 GPa [61]	0.347 [61]	9.3($\pm$0.4) s	3.3($\pm$0.1)

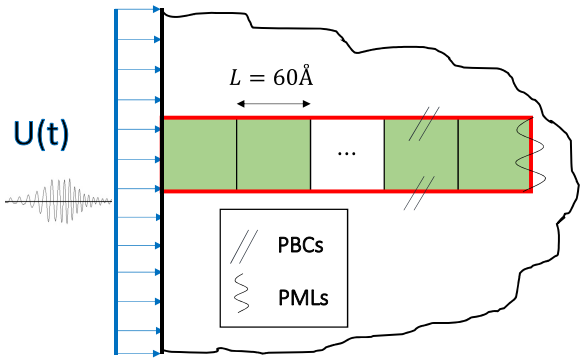

FIG. 3. 2D simulation model of solid: A semi-infinite solid can be represented by only modeling a single layer (green zone) with periodic boundary conditions (PBCs) on the top and bottom and perfectly matched layers (PMLs) on the right edge.

Once we have defined the constitutive equation [Eq. (14)] and we have calibrated our model on amorphous silicon, we can run finite-element simulations, for investigating the propagation of wave packets in large-scale materials, and compare their out-of-equilibrium attenuation with the one dictated by atomistic mechanisms.

To this aim, we prepare a system made of an horizontal line of nine squares with a side length of 60 Å, and a total length of 540 Å, as illustrated in Fig. 3. Such dimension is larger than the largest phonon mean free path at THz frequencies as reported in Ref. [20], assuring that we will be able to observe it. The size is also larger than 20 times the interatomic distance ($2 \sim 4$ Å reported in Refs. [63,64]), thus the system can be considered homogeneous and isotropic, as demonstrated in Refs. [45,46]. The system is 2D, but we generate a quasi-monochromatic acoustic pulse with plane strain state, which means that the strain along the third direction is neglected. Still, it shares the same constitutive tensor [Eq. (12)] and the same constitutive equation [Eq. (14)] with the 3D case. Details on the motion equations of the FEM simulation are reported in the Appendix.

To investigate the propagation of the vibrational energy, we excite a quasimonochromatic wave packet on the left side of the sample at position $x = 0$ in a small time interval around $t = 0$ [19]. This excitation displacement is given by

$$\mathbf{U}_\eta(t) = U_0 \times \exp\left[-\frac{(t-3t_0)^2}{2t_0^2}\right] \sin(\omega t)\mathbf{n}_\eta, \qquad (19)$$

where $U_0 = 4.9 \times 10^{-3}$ Å is a constant value, $\omega = 2\pi\nu$ is the frequency of this quasi-monochromatic excitation, and $t_0 = \frac{3\pi}{\omega}$. The direction of the applied displacement is defined by $\mathbf{n}_\eta$, which is common for all nodes on the left boundary when the excitation is coherent. The subscript η indicates the wave-packet polarization. In this case, we use $\mathbf{n}_L$ in x direction for the longitudinal polarization and $\mathbf{n}_T$ in y direction for the transverse one.

As shown in Fig. 3, periodic boundary conditions (PBCs) are applied at the top and the bottom by means of Lagrange

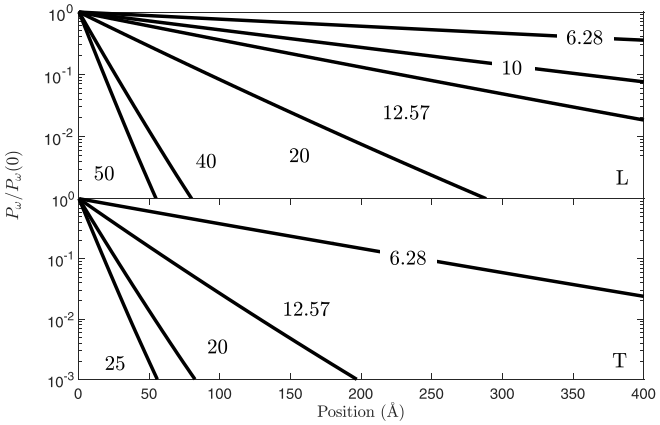

FIG. 4. Envelope of the normalized kinetic energy $P_\omega(x)/P_\omega(0)$ for different frequencies in a semilog graph. Top: longitudinal polarization; bottom: transverse polarization. Numbers near curves represent angular frequencies ω in THz.

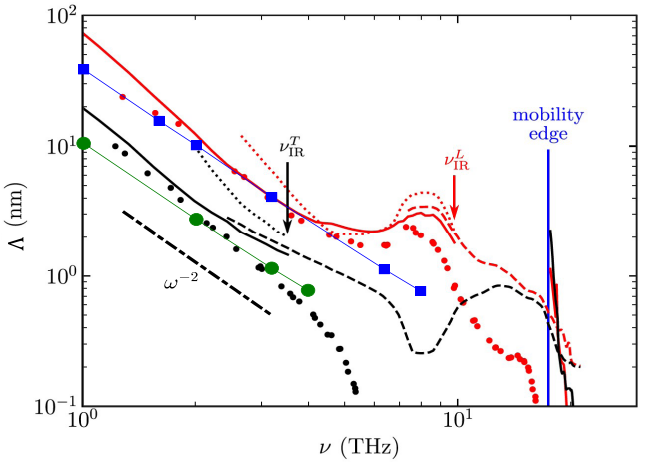

FIG. 5. Result obtained from finite-element (FE) simulation compared to atomistic analysis for longitudinal waves (blue or red) and transverse waves (green or black). For FE simulation, solid lines with large filled symbols (blue or green) show the mean free path $\Lambda_{\rm FE}$ obtained by the exponential fit of the envelope. For DM simulation (Beltukov [20]), points show the results from the DHO fit of the DSF, $\Lambda_{\rm DSF}$; solid lines show the mean free path $\Lambda_{\rm BL}$; dashed lines show the penetration length $l_{\rm pen}$. (The Ioffe-Regel frequencies for longitudinal and transverse waves are shown by red and black arrow, respectively).

multipliers $U_\eta^{\rm top} = U_\eta^{\rm bottom}$. On the right side of the model, the perfectly matched layers (PMLs) are implemented to avoid wave reflection [65–67]. Details about these two boundary conditions are presented in Ref. [68]. Moreover, plane strain state achieves the infinite length in the third direction (perpendicular to the illustrated model). Thanks to these three numerical approaches, a semi-infinite solid is represented by only modeling a single layer. Details on the space and time discretization are given in the Appendix.

IV. RESULTS

We have run a series of transient simulations, following the propagation of wave packets with energies in the THz range through a model amorphous silicon sample. As said before, the wave packet is created by imposing a displacement on the left side of the sample. Its propagation is then followed along the sample, in the x direction, which is the initial direction of propagation of the exciting wave. To investigate the acoustic attenuation due to the viscoelasticity of the medium, we measure the envelope of the kinetic energy induced in the system by the propagation of the wave packet along the x direction, and averaged over the y direction. The energy envelope is defined for each excitation frequency ω as

$$P_\omega(x) = \max_t E_k(x,t), \tag{20}$$

where $E_k(x,t)$ is the instantaneous kinetic energy supported by the frame located in x with width $\Delta x = 1$ Å. We report in Fig. 4 the normalized kinetic energy envelopes for longitudinal and transverse wave-packets. The lowest investigated frequency is $\omega = 6.28$ THz (or $\nu = 1$ THz). The maximum investigated frequency (50 THz for LA and 25 THz for TA) has been chosen slightly smaller than the Ioffe-Regel crossover for the corresponding polarization [19].

Far below the Ioffe-Regel limit, a global exponential attenuation similar to a Beer-Lambert law is observed [20,69], leading to a linear behavior in the semilog representation:

$$P_\omega(x) \propto \exp[-x/\Lambda(\omega)]. \tag{21}$$

By fitting the kinetic energy envelope with this law, one can get the value of the mean-free path $\Lambda_{\rm FE}$ (FE standing for FE simulations), which is inversely proportional to the acoustic attenuation via the wave-packet velocity. Our results for the mean free path of propagating longitudinal and transverse wave packets in amorphouos silicon are compared with results from molecular dynamics simulations [20] in Fig. 5. Here we compare with two different estimations from the atomistic calculations: $\Lambda_{\rm DSF}$ is obtained from the dynamical structure factor as detailed in Ref. [19], while $\Lambda_{\rm BL}$ has been calculated from the Beer-Lambert fit of the attenuation of propagating wave-packets. It is reported that the results of $\Lambda_{\rm DSF}$ and $\Lambda_{\rm BL}$ begin to deviate near the Ioffe-Regel frequency, which indicates a crossover from weak scattering to strong scattering. As a consequence, Beer-Lambert law gradually fails when approaching the Ioffe-Regel limit. For this reason, in Ref. [20] a penetration length is also calculated, representative of the wave-packet attenuation in the diffusive regime, $l_{\rm pen}$, such that $P_\eta(\omega, l_{\rm pen}) = \frac{1}{e}P_\eta(\omega, 0)$ [20,68], reported as well in the figure. The agreement between the mean free path from continuum finite-element simulations with the ones obtained in atomistic molecular dynamics simulations is impressive, and holds as far as we remain below the Ioffe-Regel crossover, our constitutive equation having been derived in such regime. The deviation at the highest frequencies investigated is indeed due to the approaching of the diffusive regime.

We also observe that our FE mean-free paths are closer to $\Lambda_{\rm DSF}$ rather than $\Lambda_{\rm BL}$ despite both $\Lambda_{\rm FE}$ and $\Lambda_{\rm BL}$ are fitted by the Beer-Lambert law. This is due to the fact that our model has been calibrated against the attenuation obtained form the dynamical structure factor, thus related to $\Lambda_{\rm DSF}$. That is to say, proper calibration of the parameters for the input attenuation

data will result in accurate reproduction of this attenuation when following the transient wave-packet propagation.

V. DISCUSSION

Our results demonstrate that the effective sound attenuation in a continuum model may strictly follow the atomistic quality factor Q^{-1} for a well-calibrated macroscopic linear viscoelastic constitutive law. This was proved through the relation between the attenuation Γ and the attenuation length Λ. In the damped harmonic oscillator model, Γ is proportional to the ratio of wave speed to attenuation length. If wave speed, which depends on the real part G ' of the rigidity G, keeps constant, then a macroscopic constitutive law with $\Gamma \propto \omega^2$ forces the $\lambda \propto \omega^{-2}$ behavior. This is indeed the case treated here: for the K-V model used for the hydrostatic part, real part of G is frequency-independent, but this is not true for the standard linear model used for the deviatoric part, for which the real part of G nearly doubles near the peak position. Still, the transition is too short and one can consider the real part of G as constant far from the peak, as we have done. More remarquably, we have shown in the present paper, that such a simple linear viscoelastic behavior, is sufficient to reproduce the Molecular Dynamics data obtained with a real atomistic nonequilibrium dynamics in the constant energy ensemble. This means that the relation between the apparent Γ and the mean-free path measured from wave-packet dynamics is fully coherent with a simple linear viscoelastic model, at least in the low frequency regime. More generally, our estimation of Γ results from the identification of the parameters G' and G'' of the assumed linear viscoelastic constitutive law, while the measurement of λ results from the calculation of the full out-of-equilibrium dynamics including scattering of a not strictly monochromatic wave packet at the atomic scale. By fitting the two sets of numerical data (apparent acoustic attenuation, and mean-free path of a wave packet in a given direction as a function of the frequency), we show that they are coherent with a simple continuous linear model, which opens new perspectives for effective simulations at large scales.

In the work here presented, we have developed such a law for describing acoustic attenuation in an amorphous material at THz frequencies, in a limited range below the Ioffe-Regel criterium. By choice, our model imposes a $\Gamma \propto \omega^2$ behavior, which, as mentioned in the introduction, does not hold at all frequencies. The first limitation of our model consists in the assumption of a quasi-constant speed of sound [Eq. (17)], while this is expected to be modified due to the atomic discretization and structural disorder. The second limitation is the limited frequency range of applicability. Indeed, the most interesting frequency range for the description of thermal transport in amorphous materials is actually the one around and above the Ioffe-Regel limit: when a strong scattering regime arises due to the presence of nanometric elastic heterogeneities, leading to a transition from a $\Gamma \propto \omega^4$ to $\Gamma \propto \omega^2$ behavior [17,24,27,28,30,38]. Such strong scattering and the resulting diffusive motion of initially plane waves are responsible for the plateau in the glassy thermal conductivity at around 10K, and the peak in the specific heat at the same temperature [14,70,71]. Modeling amorphous materials for thermal applications clearly needs including such frequency dependences, with at least three successive regimes including $\Gamma \propto \omega^2$, $\Gamma \propto \omega^4$ and then $\Gamma \propto \omega^2$ again at very high frequencies.

To extend the present model to larger frequency ranges, we need to describe two successive $\omega^2 - \omega^4$ crossovers, but as well to include a dispersive speed of sound, as the strong scattering leads to a strong decrease of the phonon velocity. This is the purpose of another work, which will allow to reproduce at a macroscopic level, through a single continuum model, the combined effect of parallel sources of acoustic attenuation.

Despite the present limitations, our work has the merit to be a proof of concept: by developing the appropriate viscoelastic law, and calibrating it against atomistic quantities, we are able to reproduce the correct acoustic attenuation, for both transverse and longitudinal waves. While the origin of the attenuation is microscopic, this continuum model allows reproducing it in FE simulations at a far larger scale, where the atomistic details of the material are lost. As such, our work is of evident interest in view of the current technological interests and needs. As mentioned in the introduction, for a number of different applications ranging from acoustics, to mechanical and to thermal management, complex heterogeneous materials have arisen as most promising. Such metamaterials are made of the ordered or disordered intertwinning of different materials with different properties, with a heterogeneity lengthscale (the nano- or microstructure lengthscale) which can range from macroscopic to nanometric depending on the applications. Such large scale systems can be realistically modeled only through finite-element simulations, to catch the effect of the interfaces and elastic heterogeneities on acoustic properties and thermal transport.

Until now, they have mostly been investigated by molecular dynamics simulations, allowing the investigation of the competition between the interface effect and the intrinsic acoustic attenuation as due to atomistic mechanisms. Still, the limited sample size in such simulations hinders the reproduction of the real systems and the assumption that what is observed for samples of a few tens of nanometers holds true for larger scales needs to be done [14,72–74]. In a recent work of us, we have taken the opposite approach and we have investigated the acoustic attenuation in nanocomposites through finite-element modeling, which has allowed us to model the real size materials, and study the effect of the interface scattering, highlighting the existence of propagative, diffusive and localized regime, depending on the nanostructuration lengthscale and elastic contrast between the components. Still, in that work no intrinsic acoustic attenuation was considered, the component materials being nondissipative [68]. While the viscoelastic attenuation can be taken into account by introducing a frequency-independent macroscopic viscosity [75], such description does not allow to correctly reproduce the frequency dependence of the total effective attenuation, and thus to investigate the frequency dependence of the different regimes (propagative, diffusive, localized) in the real metamaterial. With the present model, we go beyond those works, accurately reproducing the microscopic attenuation experimentally measured or obtained in atomistic calculations. As such, our model is a first decisive step to finally conjugate the two approaches, and investigate the effect of the complex

nano- or microstructure on acoustic attenuation, while including the atomistic contribution as well.

VI. CONCLUDING REMARKS

In this work we have developed a continuum mechanical model based on a viscoelastic description of an amorphous material, where the frequency dependence of the microscopic phonon attenuation can be reliably reproduced once the model has been properly calibrated on atomistic data. To do so, we have derived the analytic expression of the speed of sound and the quality factor Q^{-1}, which can be calibrated against sound velocity and attenuation as experimentally reported or calculated in atomistic numerical simulations. We have proved the validity of our approach by investigating the acoustic attenuation in amorphous silicon at THz frequencies, corresponding to phonon wavelengths in the nanometer range, where the dominant attenuation mechanism is the atomic disorder. It is worth reminding that THz acoustic phonons are the most responsible for thermal transport at room temperature. As such, our model is promising for understanding thermal transport in heterogeneous architectured materials with an amorphous component [14], most promising for thermal management applications.

While we have applied our model to the case of an amorphous material, where the intrinsic acoustic attenuation is much stronger than in crystalline materials, the approach is much more general and could be applied to crystalline materials as well, provided the viscoelastic model reproduces the microscopic attenuation, as due to anharmonic ($\Gamma \propto \omega^2$) or defects scattering ($\Gamma \propto \omega^4$). As such, this work represents a proof of concept and a first step towards a comprehensive modeling of real heterogeneous materials, where the effect of the microstructure can be modeled while accounting also for the atomistic intrinsic phonon scattering sources. From this first step, further work can focus on the reproduction of other power laws for phonon attenuation, as well as the introduction of the anisotropy, and the effect of temperature, finally allowing to describe thermal transport as well as sound propagation in metamaterials of arbitrary complexity.

APPENDIX A: 3D COMPLEX CONSTITUTIVE TENSOR

The stress-strain constitutive law describes the relation between those two quantities. Tensor can be expressed in matrix form, strain and stress are $n \times 1$ vectors, constitutive tensor is $n \times n$ matrix, where $n = d^2$, and d is dimension of space. In 3-D case, there should have been nine terms but thanks to the symmetry of shear strain $\epsilon_{ij} = \epsilon_{ji}$ and shear stress $\sigma_{ij} = \sigma_{ji}$. In Voigt notation, strain and stress vector are reduced to six terms and read, respectively:

$$\epsilon_{ij} = \begin{bmatrix} \epsilon_{11} \\ \epsilon_{22} \\ \epsilon_{33} \\ 2\epsilon_{12} \\ 2\epsilon_{13} \\ 2\epsilon_{23} \end{bmatrix} \text{ and } \sigma_{ij} = \begin{bmatrix} \sigma_{11} \\ \sigma_{22} \\ \sigma_{33} \\ \sigma_{12} \\ \sigma_{13} \\ \sigma_{23} \end{bmatrix}$$

.

It is conventional to express the shear strain as $2\epsilon_{ij} = \gamma_{ij}$, which is called engineering shear strain.

The symmetric constitutive tensor $\mathbb{G}$ ($G_{ij} = G_{ji}$) can be developed as

$$\mathbb{G} = \begin{bmatrix} G_{11} & G_{12} & G_{13} & G_{14} & G_{15} & G_{16} \\ G_{21} & G_{22} & G_{23} & G_{24} & G_{25} & G_{26} \\ G_{31} & G_{32} & G_{33} & G_{34} & G_{35} & G_{36} \\ G_{41} & G_{42} & G_{43} & G_{44} & G_{45} & G_{46} \\ G_{51} & G_{52} & G_{53} & G_{54} & G_{55} & G_{56} \\ G_{61} & G_{62} & G_{63} & G_{64} & G_{65} & G_{66} \end{bmatrix}. \tag{A1}$$

We recall that the complex constitutive law of our model (which has a form similar to Hooke's law) reads $\sigma_{ij} = E_B^* \epsilon_{ij}^{\text{sph}} + E_A^* \epsilon_{ij}^{\text{dev}}$ from which we can find each term of tensor $\mathbb{G}$, where $\epsilon_{ij}^{\text{sph}} = \frac{1}{3}\delta_{ij}(\epsilon_{11} + \epsilon_{22} + \epsilon_{33})$ and $\epsilon_{ij}^{\text{dev}} = \epsilon_{ij} - \epsilon_{ij}^{\text{sph}}$.

For example, for σ_{11},

$$\sigma_{11} = E_B^* \frac{\epsilon_{11} + \epsilon_{22} + \epsilon_{33}}{3} + E_A^* \left(\epsilon_{11} - \frac{\epsilon_{11} + \epsilon_{22} + \epsilon_{33}}{3} \right) \tag{A2}$$

$$= \frac{E_B^* + 2E_A^*}{3} \epsilon_{11} + \frac{E_B^* - E_A^*}{3} \epsilon_{22} + \frac{E_B^* - E_A^*}{3} \epsilon_{33}. \tag{A3}$$

It is easy to find that $G_{11} = \frac{E_B^* + 2E_A^*}{3}$, $G_{12} = \frac{E_B^* - E_A^*}{3}$, $G_{13} = \frac{E_B^* - E_A^*}{3}$, and $G_{14} = G_{15} = G_{16} = 0$.

Similarly, for σ_{12},

$$\sigma_{12} = E_A^* \epsilon_{12} \tag{A4}$$

$$= \frac{E_A^*}{2} \times (2\epsilon_{12}). \tag{A5}$$

So except $G_{44} = \frac{E_A^*}{2}$, other terms equal to 0.

Therefore, one can get the expression for all terms of the tensor $\mathbb{G}$ as given by Eq. (12). In addition, notice that G_{ij} is all complex number, so we use $\mathbb{G}^*$ to represent the complex constitutive tensor.

APPENDIX B: FINITE-ELEMENT SIMULATIONS DETAILS

In this work, we developed an explicit dynamic algorithm based on the finite-element code Cast3m from CEA [68,76,77]. To simplify the subscripts, we use bold symbols to represent vectors, e.g., $\sigma = \sigma_{ij}$. The finite-element semidiscrete in space of a transient dynamic motion equation can be described as

$$\boldsymbol{f}^{\text{int}}(t) + \mathbb{M}\ddot{\boldsymbol{u}}(t) = \boldsymbol{f}^{\text{ext}}(t), \tag{B1}$$

where $\boldsymbol{f}^{\text{int}}$ is internal force vector, $\mathbb{M}$ is mass matrix, $\boldsymbol{u}$ is displacement vector, and $\boldsymbol{f}^{\text{ext}}$ is exciting force vector. Among them, $\boldsymbol{f}^{\text{int}}$ can be obtained from

$$\boldsymbol{f}^{\text{int}}(t) = \int_\Omega \mathbb{B}^T \sigma(\boldsymbol{\epsilon}, \dot{\boldsymbol{\epsilon}}, \boldsymbol{h}) d\Omega, \tag{B2}$$

with

$$\boldsymbol{\epsilon}(t) = \mathbb{B}\boldsymbol{u}(t), \tag{B3}$$

where $\mathbb{B}$ is the strain-displacement matrix derived from the shape function of the element used and Ω is the model domain. The calculation of $\sigma(\boldsymbol{\epsilon}, \dot{\boldsymbol{\epsilon}}, \boldsymbol{h})$ obeys the viscoelastic constitutive law described as Eq. (14). In practice, the convolution operation in Eq. (14) is replaced by a recurrence

formula based on the internal variable $\boldsymbol{h}$ which has a "memory effect" [58,60,78–80], yielding Eq. (15). One linearization method dedicated for the generalized Maxwell viscosity derived by Kaliske *et al.* [58,60] has been implemented in this FEM code.

In the next step, we need to discretize the motion equation [Eq. (B1)] in time. We assume a uniform partition in time and choose a time step size Δt. Combined with the central-difference time integrator, the space-time discretized form can be obtained:

$$\mathbb{M}\ddot{\boldsymbol{u}}_{n+1} = \boldsymbol{f}^{\text{ext}}_{n+1} - \int_{\Omega} \mathbb{B}^T \sigma_{n+1}\left(\boldsymbol{\epsilon}_{n+1}, \dot{\boldsymbol{\epsilon}}_{n+\frac{1}{2}}, \boldsymbol{h}_{n+1}\right) d\Omega, \quad \text{(B4)}$$

where indices n and $n+1$ are successive time steps. And the derivative of strain at time $n+\frac{1}{2}$ is

$$\dot{\boldsymbol{\epsilon}}_{n+\frac{1}{2}} = \frac{1}{\Delta t}(\boldsymbol{\epsilon}_{n+1} - \boldsymbol{\epsilon}_n). \quad \text{(B5)}$$

Reference to Eq. (15), the temporally discretized constitutive law $\sigma_{n+1}(\boldsymbol{\epsilon}_{n+1}, \dot{\boldsymbol{\epsilon}}_{n+\frac{1}{2}}, \boldsymbol{h}_{n+1})$ can be expressed as a recursive equation:

$$\sigma_{n+1} = \frac{E}{1-2\nu}\left(\boldsymbol{\epsilon}^{\text{sph}}_{n+1} + \dot{\boldsymbol{\epsilon}}^{\text{sph}}_{n+\frac{1}{2}}\right) + \frac{E}{1+\nu}\boldsymbol{\epsilon}^{\text{dev}}_{n+1} + \boldsymbol{h}_{n+1}, \quad \text{(B6)}$$

where $\boldsymbol{h}_{n+1}$ is the updated internal variable tensor [58]:

$$\boldsymbol{h}_{n+1} = \exp\left(-\frac{\Delta t}{\tau_a}\right)\boldsymbol{h}_n + \frac{E}{1+\nu}\tau_a\left[1 - \exp\left(-\frac{\Delta t}{\tau_a}\right)\right]\dot{\boldsymbol{\epsilon}}^{\text{dev}}_{n+\frac{1}{2}}. \quad \text{(B7)}$$

To resume, the right-hand side of Eq. (B6) shows that the updated stress consists of three part: (1) $\boldsymbol{\epsilon}$ gives the purely elastic stress; (2) $\dot{\boldsymbol{\epsilon}}$ gives the viscous stress at the current time step; (3) $\boldsymbol{h}$ records the time-dependent relaxation process. For more details about the implemented central-difference time integrator algorithm, see Ref. [68].

1. Spatial discretization

It is clear that the element size in element-based acoustic computations should be related to the wavelength. A common rule is that at least six linear elements should be used per wavelength [81]. In this work, we use the P-1 element which is quadrangle shape and has four nodes on the corners. The reference length of spatial discretization is 1 Å for the reference frequency $\omega_{\text{ref}} = 6.28$ THz, which means that transverse wave has approximate 40 elements per wavelength. As the frequency increases and the wavelength becomes shorter, we have refined the mesh size accordingly.

2. Time integration

Among all the FEM time integration schemes, Newmark scheme [82] is the most common solution for a dynamic structure. We have selected the symplectic central-difference algorithm from the Newmark scheme family, in that case $\gamma = \frac{1}{2}$ and $\beta = 0$. The time step Δt should satisfy the convergence condition: $\Delta t < \Delta t_{\text{cr}}$ and the critical time step $\Delta t_{cr} = \frac{\Delta l}{v_{\text{wave}}}$ where Δl is linked to mesh size and v_{wave} is defined by P-wave celerity. Based on that, the time step of simulation is $\Delta t \sim 1$ fs for 6.28 THz and becomes shorter with increasing frequency. Total simulation time is more than 10^4 fs to make sure that the wave packet passes through the sample.

[1] O. Bouaziz, Y. Bréchet, and J. Embury, Heterogeneous and architectured materials: A possible strategy for design of structural materials, Adv. Eng. Mater. **10**, 24 (2008).

[2] Z. Liu, Locally resonant sonic materials, Science **289**, 1734 (2000).

[3] A. Khelif, B. Aoubiza, S. Mohammadi, A. Adibi, and V. Laude, Complete band gaps in two-dimensional phononic crystal slabs, Phys. Rev. E **74**, 046610 (2006).

[4] S. Zhang, L. Yin, and N. Fang, Focusing Ultrasound with an Acoustic Metamaterial Network, Phys. Rev. Lett. **102**, 194301 (2009).

[5] S. A. Cummer, J. Christensen, and A. Alù, Controlling sound with acoustic metamaterials, Nat. Rev. Mater. **1**, 16001 (2016).

[6] S. Lee, B. Kang, H. Keum, N. Ahmed, J. A. Rogers, P. M. Ferreira, S. Kim, and B. Min, Heterogeneously assembled metamaterials and metadevices via 3D modular transfer printing, Sci. Rep. **6**, 27621 (2016).

[7] G. Park, S. Kang, H. Lee, and W. Choi, Tunable multifunctional thermal metamaterials: Manipulation of local heat flux via assembly of unit-cell thermal shifters, Sci. Rep. **7**, 41000 (2017).

[8] S. R. Sklan and B. Li, Thermal metamaterials: Functions and prospects, Natl. Sci. Rev. **5**, 138 (2018).

[9] M. I. Hussein, C.-N. Tsai, and H. Honarvar, Nanophononics: Thermal conductivity reduction in a nanophononic metamaterial versus a nanophononic crystal: A review and comparative analysis, Adv. Funct. Mater. **30**, 2070047 (2020).

[10] D. J. R. Geradin, *Mechanical Vibrations: Theory and Application to Structural Dynamics*, 3rd ed. (John Wiley & Sons, New York, 2014).

[11] T. Belytschko, W. K. Liu, B. Moran, and K. Elkhodary, *Nonlinear Finite Elements for Continua and Structures* (Wiley John & Sons, New York, 2013).

[12] M. Bonnet, A. Frangi, and C. Rey, *The Finite Element Method in Solid Mechanics* (McGraw Hill Education, New York, 2014).

[13] J. Achenbach, *Wave Propagation in Elastic Solids*, Vol. 16 (Elsevier, Amsterdam, 2012).

[14] A. Tlili, V. M. Giordano, Y. M. Beltukov, P. Desmarchelier, S. Merabia, and A. Tanguy, Enhancement and anticipation of the Ioffe–Regel crossover in amorphous/nanocrystalline composites, Nanoscale **11**, 21502 (2019).

[15] K. S. Gilroy and W. A. Phillips, An asymmetric double-well potential model for structural relaxation processes in amorphous materials, Philos. Mag. B **43**, 735 (1981).

[16] W. Ji, M. Popovic, T. W. J. de Geus, E. Lerner, and M. Wyart, Theory for the density of interacting quasilocalized modes in amorphous solids, Phys. Rev. E **99**, 023003 (2019).

[17] S. Ayrinhac, M. Foret, A. Devos, B. Ruffle, E. Courtens, and R. Vacher, Subterahertz hypersound attenuation in silica glass studied via picosecond acoustics, Phys. Rev. B **83**, 014204 (2011).

[18] U. Buchenau, Y. M. Galperin, V. L. Gurevich, D. A. Parshin, M. A. Ramos, and H. R. Schober, Interaction of soft modes and sound waves in glasses, Phys. Rev. B **46**, 2798 (1992).

[19] Y. M. Beltukov, C. Fusco, D. A. Parshin, and A. Tanguy, Boson peak and Ioffe-Regel criterion in amorphous siliconlike materials: The effect of bond directionality, Phys. Rev. E **93**, 023006 (2016).

[20] Y. M. Beltukov, D. A. Parshin, V. M. Giordano, and A. Tanguy, Propagative and diffusive regimes of acoustic damping in bulk amorphous material, Phys. Rev. E **98**, 023005 (2018).

[21] S. Gelin, H. Tanaka, and A. Lemaître, Anomalous phonon scattering and elastic correlations in amorphous solids, Nat. Mater. **15**, 1177 (2016).

[22] T. Damart, A. Tanguy, and D. Rodney, Theory of harmonic dissipation in disordered solids, Phys. Rev. B **95**, 054203 (2017).

[23] B. Rufflé, M. Foret, E. Courtens, R. Vacher, and G. Monaco, Observation of the Onset of Strong Scattering on High-Frequency Acoustic Phonons in Densified Silica Glass, Phys. Rev. Lett. **90**, 095502 (2003).

[24] B. Rufflé, G. Guimbretière, E. Courtens, R. Vacher, and G. Monaco, Glass-Specific Behavior in the Damping of Acoustic-like Vibrations, Phys. Rev. Lett. **96**, 045502 (2006).

[25] B. Rufflé, D. A. Parshin, E. Courtens, and R. Vacher, Boson Peak and its Relation to Acoustic Attenuation in Glasses, Phys. Rev. Lett. **100**, 015501 (2008).

[26] C. Levelut, R. Le Parc, and J. Pelous, Dynamic sound attenuation at hypersonic frequencies in silica glass, Phys. Rev. B **73**, 052202 (2006).

[27] G. Monaco and V. M. Giordano, Breakdown of the Debye approximation for the acoustic modes with nanometric wavelengths in glasses, Proc. Natl. Acad. Sci. U.S.A. **106**, 3659 (2009).

[28] G. Baldi, V. M. Giordano, G. Monaco, and B. Ruta, Sound Attenuation at Terahertz Frequencies and the Boson Peak of Vitreous Silica, Phys. Rev. Lett. **104**, 195501 (2010).

[29] E. Duval and A. Mermet, Inelastic x-ray scattering from non-propagating vibrational modes in glasses, Phys. Rev. B **58**, 8159 (1998).

[30] H. Mizuno, S. Mossa, and J.-L. Barrat, Acoustic excitations and elastic heterogeneities in disordered solids, Proc. Natl. Acad. Sci. U.S.A. **111**, 11949 (2014).

[31] A. Tanguy, J. P. Wittmer, F. Leonforte, and J.-L. Barrat, Continuum limit of amorphous elastic bodies: A finite-size study of low-frequency harmonic vibrations, Phys. Rev. B **66**, 174205 (2002).

[32] F. Leonforte, A. Tanguy, J. P. Wittmer, and J.-L. Barrat, Inhomogeneous Elastic Response of Silica Glass, Phys. Rev. Lett. **97**, 055501 (2006).

[33] A. Tanguy, B. Mantisi, and M. Tsamados, Vibrational modes as a predictor for plasticity in a model glass, Europhys. Lett. **90**, 16004 (2010).

[34] A. Marruzzo, W. Schirmacher, A. Fratalocchi, and G. Ruocco, Heterogeneous shear elasticity of glasses: The origin of the boson peak, Sci. Rep. **3**, 1407 (2013).

[35] W. Schirmacher, T. Scopigno, and G. Ruocco, Theory of vibrational anomalies in glasses, J. Non-Cryst. Solids **407**, 133 (2015).

[36] G. Monaco and S. Mossa, Anomalous properties of the acoustic excitations in glasses on the mesoscopic length scale, Proc. Natl. Acad. Sci. U.S.A. **106**, 16907 (2009).

[37] L. Wang, L. Berthier, E. Flenner, P. Guan, and G. Szamel, Sound attenuation in stable glasses, Soft Matter **15**, 7018 (2019).

[38] H. Mizuno, G. Ruocco, and S. Mossa, Sound damping in glasses: Interplay between anharmonicities and elastic heterogeneities, Phys. Rev. B **101**, 174206 (2020).

[39] P. B. Allen, J. L. Feldman, J. Fabian, and F. Wooten, Diffusons, locons and propagons: Character of atomic vibrations in amorphous Si, Philos. Mag. B **79**, 1715 (1999).

[40] E. van der Giessen, P. A. Schultz, N. Bertin, V. V. Bulatov, W. Cai, G. Csányi, S. M. Foiles, M. G. D. Geers, C. González, M. Hütter, W. K. Kim, D. M. Kochmann, J. LLorca, A. E. Mattsson, J. Rottler, A. Shluger, R. B. Sills, I. Steinbach, A. Strachan, and E. B. Tadmor, Roadmap on multiscale materials modeling, Modell. Simul. Mater. Sci. Eng. **28**, 043001 (2020).

[41] V. Bulatov and A. Argon, A stochastic model for continuum elastoplastic behavior. I. Numerical approach and strain localization, Modell. Simul. Mater. Sci. Eng. **2**, 167 (1994).

[42] C. Maloney and A. Lemaître, Universal Breakdown of Elasticity at the Onset of Material Failure, Phys. Rev. Lett. **93**, 195501 (2004).

[43] T. Albaret, A. Tanguy, F. Boioli, and D. Rodney, Mapping between atomistic simulations and eshelby inclusions in the shear deformation of an amorphous silicon model, Phys. Rev. E **93**, 053002 (2016).

[44] A. Nicolas, E. E. Ferrero, K. Martens, and J.-L. Barrat, Deformation and flow of amorphous solids: Insights from elastoplastic models, Rev. Mod. Phys. **90**, 045006 (2018).

[45] M. Tsamados, A. Tanguy, C. Goldenberg, and J.-L. Barrat, Local elasticity map and plasticity in a model Lennard-Jones glass, Phys. Rev. E **80**, 026112 (2009).

[46] G. Molnár, P. Ganster, J. Török, and A. Tanguy, Sodium effect on static mechanical behavior of MD-modeled sodium silicate glasses, J. Non-Cryst. Solids **440**, 12 (2016).

[47] G. Molnar, P. Ganster, and A. Tanguy, Effect of composition and pressure on the shear strength of sodium silicate glasses: An atomic scale simulation study, Phys. Rev. E **95**, 043001 (2017).

[48] G. Molnár, P. Ganster, A. Tanguy, E. Barthel, and G. Kermouche, Densification dependent yield criteria for sodium silicate glasses—An atomistic simulation approach, Acta Mater. **111**, 129 (2016).

[49] G. Molnár, G. Kermouche, and E. Barthel, Plastic response of amorphous silicates, from atomistic simulations to experiments—A general constitutive relation, Mech. Mater. **114**, 1 (2017).

[50] J. R. Willis, The construction of effective relations for waves in a composite, C. R. Mec. **340**, 181 (2012).

[51] G. G. Stokes, On the theories of the internal friction of fluids in motion, and of the equilibrium and motion of elastic solids, in *Mathematical and Physical Papers*, Cambridge Library Collection - Mathematics (Cambridge University Press, Cambridge, 2009), pp. 75–129.

[52] R. O. Pohl, X. Liu, and E. Thompson, Low-temperature thermal conductivity and acoustic attenuation in amorphous solids, Rev. Mod. Phys. **74**, 991 (2002).
[53] W. Schirmacher, The boson peak, Phys. Status Solidi B **250**, 937 (2013).
[54] S. Parke, Logarithmic decrements at high damping, Br. J. Appl. Phys. **17**, 271 (1966).
[55] M. Carfagni, E. Lenzi, and M. Pierini, The loss factor as a measure of mechanical damping, in *Proceedings of the 16th International Modal Analysis Conference*, Society of Photo-Optical Instrumentation Engineers (SPIE) Conference Series Vol. 3243 (SPIE, 1998), p. 580.
[56] J. C. Maxwell *et al.*, IV. On the dynamical theory of gases, Philos. Trans. R. Soc. London **157**, 49 (1867).
[57] D. Roylance, *Engineering Viscoelasticity (Department of Materials Science and Engineering–Massachusetts Institute of Technology* (Cambridge, MA, 2001), Vol. 2139, pp. 1–37.
[58] M. Kaliske and H. Rothert, Formulation and implementation of three-dimensional viscoelasticity at small and finite strains, Comput. Mech. **19**, 228 (1997).
[59] Y. Feng, J. Goree, and B. Liu, Longitudinal viscosity of two-dimensional Yukawa liquids, Phys. Rev. E **87**, 013106 (2013).
[60] M. Kaliske, A formulation of elasticity and viscoelasticity for fibre reinforced material at small and finite strains, Comput. Methods Appl. Mech. Eng. **185**, 225 (2000).
[61] C. Fusco, T. Albaret, and A. Tanguy, Role of local order in the small-scale plasticity of model amorphous materials, Phys. Rev. E **82**, 066116 (2010).
[62] F. H. Stillinger and T. A. Weber, Computer simulation of local order in condensed phases of silicon, Phys. Rev. B **31**, 5262 (1985).
[63] T. Vazhappilly and D. A. Micha, Atomic modeling of structural and optical properties of amorphous silicon, Chem. Phys. Lett. **570**, 95 (2013).
[64] A. M. Ukpong, Studies of the electronic and vibrational signatures of the unusual bonding geometries in melt-quenched amorphous silicon, Mol. Phys. **107**, 2521 (2009).
[65] J. Lysmer and R. L. Kuhlemeyer, Finite dynamic model for infinite media, J. Eng. Mech. Div. **95**, 859 (1969).
[66] R. Clayton and B. Engquist, Absorbing boundary conditions for acoustic and elastic wave equations, Bull. Seismol. Soc. Am. **67**, 1529 (1977).
[67] H. S. Kim, A study on the performance of absorbing boundaries using dashpot, Engineering **06**, 593 (2014).
[68] H. Luo, A. Gravouil, V. Giordano, and A. Tanguy, Thermal transport in a 2D nanophononic solid: Role of bi-phasic materials properties on acoustic attenuation and thermal diffusivity, Nanomaterials **9**, 1471 (2019).
[69] D. F. Swinehart, The Beer-Lambert law, J. Chem. Edu. **39**, 333 (1962).
[70] R. Zeller and R. Pohl, Thermal conductivity and specific heat of noncrystalline solids, Phys. Rev. B **4**, 2029 (1971).
[71] R. Pohl, Amorphous materials: Thermal conductivity, in *Encyclopedia of Materials: Science and Technology* (Elsevier, Amsterdam, 2001), pp. 232–237.
[72] W. Li, Y. Yang, G. Zhang, and Y.-W. Zhang, Ultrafast and directional diffusion of lithium in phosphorene for high-performance lithium-ion battery, Nano Lett. **15**, 1691 (2015).
[73] L. Yang, N. Yang, and B. Li, Extreme low thermal conductivity in nanoscale 3D Si phononic crystal with spherical pores, Nano Lett. **14**, 1734 (2014).
[74] T. Damart, V. M. Giordano, and A. Tanguy, Nanocrystalline inclusions as a low-pass filter for thermal transport in a-Si, Phys. Rev. B **92**, 094201 (2015).
[75] Y.-F. Wang, Y.-S. Wang, and V. Laude, Wave propagation in two-dimensional viscoelastic metamaterials, Phys. Rev. B **92**, 104110 (2015).
[76] P. Verpeaux, A. Millard, T. Charras, and A. Combescure, *A Modern Approach of Large Computer Codes for Structural Analysis* (IASMiRT, Anaheim, CA, 1989).
[77] M.-É. Schwaab, T. Biben, S. Santucci, A. Gravouil, and L. Vanel, Interacting Cracks Obey a Multiscale Attractive to Repulsive Transition, Phys. Rev. Lett. **120**, 255501 (2018).
[78] S. Reese and S. Govindjee, A theory of finite viscoelasticity and numerical aspects, Int. J. Solids Struct. **35**, 3455 (1998).
[79] R. Lin and U. Schomburg, A finite elastic–viscoelastic–elastoplastic material law with damage: Theoretical and numerical aspects, Comput. Methods Appl. Mech. Eng. **192**, 1591 (2003).
[80] L. Rouleau and J.-F. Deü, Time-domain analysis of viscoelastic systems, Procedia Eng. **199**, 384 (2017).
[81] S. Marburg and B. Nolte (eds.), *Computational Acoustics of Noise Propagation in Fluids—Finite and Boundary Element Methods* (Springer, Berlin, Heidelberg, 2008).
[82] N. M. Newmark, A method of computation for structural dynamics, J. Eng. Mech. Div. **85**, 67 (1959).